Benchmarking Dielectronic Recombination Rate Coefficients for Carbon-like Ca^{14+}

C. Y. Zhang[1,2] , B. S. Yan[2] , K. Wang[3,4] , R. Si[2], K. Yao[2] , W. L. Ma[5], Z. K. Huang[6], W. Q. Wen[6] , X. W. Ma[6] ,
L. F. Zhu[5] , C. Y. Chen[2], and N. R. Badnell[1]

[1] Department of Physics, University of Strathclyde, Glasgow, G4 0NG, UK; chunyu.zhang@strath.ac.uk

[2] Shanghai EBIT Lab, Key Laboratory of Nuclear Physics and Ion-beam Application, Institute of Modern Physics, Department of Nuclear Science and Technology,
Fudan University, Shanghai 200433, People's Republic of China; rsi@fudan.edu.cn

[3] Department of Physics and Anhui Key Laboratory of Optoelectric Materials Science and Technology, Key Laboratory of Functional Molecular Solids, Ministry of
Education, Anhui Normal University, Wuhu, Anhui 241000, People's Republic of China

[4] Hebei Key Lab of Optic-electronic Information and Materials, The College of Physics Science and Technology, Hebei University, Baoding 071002, People's
Republic of China

[5] Department of Modern Physics, University of Science and Technology of China, Hefei, Anhui 230026, People's Republic of China

[6] Institute of Modern Physics, Chinese Academy of Sciences, Lanzhou 730000, People's Republic of China

Received 2024 February 27; revised 2024 August 30; accepted 2024 September 26; published 2024 November 14

Abstract

Dielectronic recombination (DR) rate coefficients for C-like Ca^{14+} were measured by Wen et al. at the electron cooler storage ring in Lanzhou, China. The measured DR rate coefficients from 0 to 92 eV cover most of the DR resonances associated with the $2s^2 2p^2 \rightarrow 2s^2 2p^2$ and $2s^2 2p^2 \rightarrow 2s 2p^3$ core transitions. In addition, Wen et al. reported theoretical results calculated with the Flexible Atomic Code (FAC) and AUTOSTRUCTURE (AS). However, these theoretical results show widespread and significant differences from the measured DR spectrum in both resonance energies and strengths, as well as between each other. In the present work, we uncover the reasons behind these large differences, both theoretical and experimental. The new FAC and AS results reproduce the observed spectrum in detail, especially at resonance energies below 8 eV, and they are in very close agreement with each other. The present plasma rate coefficients agree with the experimentally determined values to within 20% and 2% in the photoionized plasma (PP) and collisional ionized plasma (CP) temperature ranges, respectively. This is in contrast to the previous theoretical results, which showed differences with the experiment of up to ∼40% over the PP temperature range. The present FAC and AS results agree with each other within 5% in the PP and CP temperature ranges. Thus, the theoretical uncertainty is greatly reduced for the DR of Ca^{14+} and the present benchmarking with the experiment gives confidence to data users modeling non–local thermodynamic equilibrium plasma.

Unified Astronomy Thesaurus concepts: Atomic data (2216); Atomic data benchmarking (2064); Plasma astrophysics (1261); Collisional processes (2286); Atomic physics (2063)

1. Introduction

The high-resolution X-Ray Imaging and Spectroscopy Mission (XRISM) satellite (M. Tashiro et al. 2018) was launched recently. Its spectroscopic capability will significantly advance our ability with the identification of specific emission lines associated with elements in different ionization states (M. Tashiro et al. 2018). However, the X-ray spectra of the Perseus galaxy cluster, as observed by Hitomi (Hitomi Collaboration et al. 2016), have shown the pressing need for substantial improvements in the currently used atomic databases and models (Hitomi Collaboration et al. 2017, 2018). This necessity stems from the intricate task of analyzing and modeling the high-resolution spectra of cosmic atomic plasmas, which requires a deep and precise understanding of the microphysical processes that produce the observed spectra (M. Schnell et al. 2003; N. R. Badnell 2006; G. D. Zanna & H. E. Mason 2018; K. P. Dere et al. 2019). Furthermore, ionization balance calculations for both photoionized plasmas (PPs) and collisionally ionized plasmas (CPs; T. R. Kallman & P. Palmeri 2007; P. Bryans et al. 2009) depend on accurate ionization and recombination data. Dielectronic recombination (DR), an electron–ion interaction process, where a low-energy electron resonantly

excites an ion and radiationlessly moves into an autoionizing state of the recombining ion, is generally the dominant recombination mechanism for most ions in low-density plasmas (A. Burgess 1964; M. Schnell et al. 2003; N. R. Badnell 2006; P. Bryans et al. 2006; G. D. Zanna & H. E. Mason 2018). The requirement for DR data with less uncertainty becomes even bigger as we look forward to the upcoming XRISM measurements.

Modelers currently depend on software packages such as AtomDB (A. R. Foster et al. 2012), CHIANTI (K. P. Dere et al. 2019; G. Del Zanna et al. 2021), CLOUDY (G. J. Ferland et al. 1998), and XSTAR (M. A. Bautista & T. R. Kallman 2001) for diagnosing astrophysical spectra. DR data calculated by the AUTOSTRUCTURE (AS) code (N. R. Badnell et al. 2003; N. R. Badnell 2011) available on the UK APAP website[7] is widely used in these sources. AS (N. R. Badnell et al. 2003; N. R. Badnell 2011) was developed by N. R. Badnell and used to perform kappa-averaged semirelativistic distorted-wave (SRDW) DR calculations (J. Colgan et al. 2003, 2004; O. Zatsarinny et al. 2003, 2004a, 2004b, 2006; Z. Altun et al. 2004; D. M. Mitnik & N. R. Badnell 2004) for highly charged ions (HCIs) with an open L-shell. Moreover, M. F. Gu developed the Flexible Atomic Code (FAC)[8] to perform

---

[7] UK APAP network: http://apap-network.org.

[8] FAC2: https://github.com/flexible-atomic-code/fac/tree/svn/tags/fac-1_1_1.

relativistic distorted-wave (RDW) DR calculations (M. F. Gu 2003) for L-shell HCIs. These theoretical plasma rate coefficients are usually lower than experimentally derived ones, by ∼30% in the PP and CP temperature ranges (M. Schnell et al. 2003; S. Schippers et al. 2004; I. Orban et al. 2008, 2010; Z. K. Huang et al. 2018; S. X. Wang et al. 2018) or even up to ∼40% for AS results deviating from the experiment (W. Q. Wen et al. 2020).

The accuracy of DR rate coefficients from AS and FAC calculations for PP application has encountered a bottleneck, being stuck at this level for the past 20 yr. The PP temperatures are much lower than those in CP, and DR takes place through low-lying resonances that are only described by challenging atomic structure calculations (M. Schnell et al. 2003; N. R. Badnell 2007; C. Y. Zhang et al. 2023). As a result, interpreting PP spectra faces great challenges. In recent years, we have collaborated closely with the research group at the cooler storage ring in Lanzhou, China, to study the DR rate coefficients for many L-shell HCIs (Z. K. Huang et al. 2018; N. Khan et al. 2018; S. X. Wang et al. 2018, 2019; S. Mahmood et al. 2020; W. Q. Wen et al. 2020), by using FAC (M. F. Gu 2008) and AS (N. R. Badnell 2011). For these L-shell ions, theoretical plasma rate coefficients are usually lower than the experimental ones. Only configuration interaction (CI) among DR resonances with the same principal quantum numbers n for the captured electrons (single-n CI) was considered in our previous calculations. As discussed in detail in our recent work for Be-like Ar^{14+} (C. Y. Zhang et al. 2023), by considering more configuration mixing, via CI among DR resonances with different principal quantum numbers n for the captured electrons (multi-n CI), FAC and AS plasma rate coefficients can be brought into agreement with experimentally derived values (Z. K. Huang et al. 2018), to within ∼10% in the PP and CP temperature ranges. This is a significant improvement, compared with the ∼30% difference between previous FAC/AS calculations and experiments, as mentioned above.

In this work, we continue to explore strategies to improve the calculated accuracy for low-energy resonances in C-like Ca^{14+}. Using two different codes, i.e., FAC (M. F. Gu 2008) and AS (N. R. Badnell 2011), we investigate the DR rate coefficients within $\Delta n = 0$ for C-like Ca^{14+} from the initial ground state ($1s^2 2s^2 2p^2 \, ^3P_0$). Moreover, we analyze in detail the influence of radial potential, multi-n CI, and the autoionization data of low-lying states. The present FAC and AS results agree much better with the measured spectrum (W. Q. Wen et al. 2020) than previous calculations. The present FAC and AS plasma rate coefficients agree with each other within 5% at PP and CP temperatures. They agree with the experimentally deduced ones (W. Q. Wen et al. 2020) within 20% and 2% at PP and CP temperatures, respectively. However, the previous theoretical calculations (W. Q. Wen et al. 2020) are lower than the measurement by up to ∼40%.

The remainder of this paper is organized as follows. The calculational procedure is outlined in Section 2. In Section 3, we present our FAC and AS results for Ca^{14+} and compare them with measured spectra and existing theoretical calculations. Moreover, the effects of atomic radial potential, autoionization transitions near the threshold, and multi-n CI are discussed in detail. A conclusion is given in Section 4.

2. Outline of Theory and Calculational Procedure

We give an outline of the theory of the distorted-wave approach used here. The details can be found in N. R. Badnell (2006). For descriptions of the FAC and AS codes, the reader should consult M. F. Gu (2008) and N. R. Badnell (2011).

In the independent processes and isolated resonance approximations (M. S. Pindzola et al. 1992; N. R. Badnell 2006), the DR resonance strengths can be obtained by using the principle of detailed balance for the dielectronic capture, to give

$$S_{ij} = \frac{(2\pi I_H a_0)^2 \tau_0}{E_{ij}} \frac{g_j}{2g_i} A_{ji}^a B_j^r, \tag{1}$$

where i represents the initial level of the recombining ion (C-like) in the resonance capture process, j represents the resulting unstable doubly or triply excited intermediate level, and g_i and g_j are statistical weights of the i and j levels, respectively. A_{ji}^a is the autoionization rate from j to i. $E_{ij} = E_j – E_i$ represents the resonance energy, which is fixed by the position of the resonance j relative to the continuum i. It should be noted that the DR process is resonant and it occurs only when the kinetic energy of the incident electron matches with the resonance energy E_{ij}. I_H is the ionization potential energy of the hydrogen atom. Both E_{ij} and I_H are in the same units of energy: $(2\pi a_0)^2 \tau_0 = 2.6741 \times 10^{-32}$ cm^2 s.

B_j^r represents the DR radiative branching ratio, which can be defined as

$$B_j^r = \frac{\sum_f A_{jf}^r}{\sum_k A_{jk}^a + \sum_h A_{jh}^r}, \tag{2}$$

where k represents all possible final autoionizing states from j, f represents the bound levels in the recombined ion (N-like), and h represents all possible final states of radiative decay.

When the radiative decays to autoionizing levels, followed by radiative cascade (DAC) channels being included, B_j^r should be rewritten as

$$B_j'^r = \frac{\sum_f A_{jf}^r + \sum_{j'} A_{jj'}^r B_{j'}'^r}{\sum_k A_{jk}^a + \sum_h A_{jh}^r}, \tag{3}$$

where j' are lower-lying ($j' < j$) autoionizing levels that then radiatively cascade through the levels of the recombined ion (N-like). Here, $\sum_h A_{jh}^r = \sum_f A_{jf}^r + \sum_{j'} A_{jj'}^r$. $B_{j'}'^r$ indicates the DR radiative branching ratio of state j' and it is defined in the same way as in Equation (3).

Summing over all possible autoionization channels, j, and averaging over the Maxwellian distribution of the free electron energy, the plasma rate coefficients for thermal equilibrium plasmas can be given as (A. Burgess 1964)

$$\alpha(T_e) = \left(\frac{4\pi a_0^2 I_H}{k_B T_e}\right)^{3/2} \sum_j \frac{g_j}{2g_i} A_{ji}^a B_j^r \exp\left(-\frac{E_{ij}}{k_B T_e}\right), \tag{4}$$

where k_B represents the Boltzmann constant and $(4\pi a_0^2)^{3/2} = 6.6011 \times 10^{-24}$ cm^3.

The measured rate coefficients within $\Delta n = 0$ channels cover most of the DR resonances associated with the $2s^2 2p^2 \rightarrow$

$2s^22p^2$ and $2s^22p^2 \rightarrow 2s2p^3$ core transitions (W. Q. Wen et al. 2020). In order to compare with the observed spectrum (W. Q. Wen et al. 2020), the $n = 2 \rightarrow 2$ core excitation channels are considered in the present FAC and AS calculations. The autoionization and radiative decay transitions involved in the present calculations can be represented as:

$$e^- + 1s^22s^22p^2 \rightarrow 1s^22l''^4nl \rightarrow 1s^22l''^3n'l' + e^-,$$

$$\searrow \begin{Bmatrix} 1s^22l'''^4nl \\ 1s^22l''^4n''l''' \end{Bmatrix} + h\nu, \quad (5)$$

where $n \leqslant 75$, $l \leqslant 12$, $n' \leqslant 10$, $l' \leqslant 9$, $l'' \leqslant 1$, $l''' \leqslant 1$, $n'' \leqslant 75$, and $l'''' \leqslant 12$.

To determine the reason(s) behind the large discrepancies between the previous FAC/AS results and the experimental spectra for Ca^{14+} (W. Q. Wen et al. 2020), we performed three different FAC calculations: a repeat of the old calculation (W. Q. Wen et al. 2020) and two new ones, considering only single-nl CI and additionally including multi-n CI, detailed below. The same three calculations were also carried out using AS. We consider the same CI expansion in the FAC and AS calculations. These calculations are labeled as

1. *Old FAC.* The unique radial orbital potential was generated from all possible $1s^22l^4 (l \leqslant 1)$ configurations in the *recombining* (C-like) ion. The CI among $1s^22l'^4nl$ ($l' \leqslant 1$, $n \leqslant 10$, $l \leqslant 9$) was restricted to within the same n and same l (single-nl CI) for the recombined (N-like) ion.
2. *New FAC single-nl CI.* The radial potential generated from all possible $1s^22l^5 (l \leqslant 1)$ configurations in the *recombined* (N-like) ion is used. The same single-nl CI as the old FAC calculation is used.
3. *New FAC multi-n CI.* The same radial potential was used as the new FAC single-nl CI calculation. The CI among all possible $1s^22l'^4nl$ ($l' \leqslant 1$, $n \leqslant 10$, $l \leqslant 9$; multi-n CI) is considered for the recombined (N-like) ion.
4. *Old AS.* The same single-nl CI as with the old FAC calculation is considered. In some cases, where the calculated energy splittings are smaller than observed, the ionization limit should be lowered slightly in the AS calculation, to ensure that all potential autoionization data exist for low-lying autoionizing states (hereafter, a pre-drop of the ionization limit, for short). It may be discarded later in a postprocessor, by further application of observed/accurate theoretical energies. However, this was not done in W. Q. Wen et al. (2020).
5. *New AS single-nl CI.* The same single-nl CI as with the new FAC single-nl CI calculation is considered. Low-lying resonances lost in the old AS calculation are now included by a pre-drop of the ionization limit.
6. *New AS multi-n CI.* The same multi-n CI as with the new FAC multi-n CI calculation is considered. Low-lying resonances lost in the old AS calculation are now included by a pre-drop of the ionization limit.

In FAC, a unique Dirac–Fock–Slater radial potential is generated, based on a fictitious mean configuration with fractional occupation numbers that define this configuration, representing the average electron cloud of the configurations in calculations (M. F. Gu 2008). Users can specify the occupation numbers of this mean potential, which is employed to describe both the recombining ion (e.g., Ca^{14+}) and the recombined ion (e.g., Ca^{13+}) in all FAC calculations (M. F. Gu 2008). Please note that the actual "working" equations of potential used in the current FAC code[9] should be seen in N. R. Badnell & C. Y. Zhang (2024).

Electric-dipole (E1) radiative rates and autoionization rates involving the $n \leqslant 75$ ($l \leqslant 12$) levels are explicitly calculated by the relativistic configuration interaction (RCI) method. The contributions of the $75 < n \leqslant 1000$ ($l \leqslant 12$) resonances for plasma rate coefficients are included via the level-by-level extrapolation method, as discussed in A. Peleg et al. (1998) and F.-C. Meng et al. (2007).

In the present AS calculations, Slater-type orbital (STO) potentials (A. Burgess et al. 1989) and a relaxed (RLX) orbital basis are used to describe the recombining ion (Ca^{14+}) and recombined ion (Ca^{13+}) independently. By RLX, we mean that each (nl) configuration is described by its own set of orbitals, where each electron moves in a potential built from STOs and occupation numbers for all other electrons present in the same configuration. Thus, in general, the orbitals are nonorthogonal and the radial overlaps are taken to be zero or unity—this is the same approach as taken by Cowan's Hartree–Fock relativistic code (R. D. Cowan 1981). Excitation energies, E1 radiative rates, and autoionization rates involving the $n \leqslant 10$ ($l \leqslant 9$) levels are calculated in the intermediate-coupling scheme with the multiconfiguration Breit–Pauli (MCBP) approximation. The single-nl radiative rates and autoionization rates for the high-lying $11 \leqslant n \leqslant 100$ ($l \leqslant 12$) resonances are calculated in the same fashion but with CI within the C-like core only. The single-nl rates for higher n up to 1000 are calculated using a quasi-logarithmically spaced set of n-values, and interpolation is then used to obtain the remaining n.

The present resonance energies (with $n \geqslant 6$) are estimated by a Rydberg formula (RF) that treats the Rydberg electron hydrogenically:

$$E_{nl} = E_{exc} - R \left(\frac{z}{n - \mu_l} \right)^2, \quad (6)$$

where E_{nl} is the resonance energy for a given nl state, E_{exc} is the core excitation energy, z is the charge state of the recombining ion, R is the Rydberg energy, and μ_l is the quantum defect (R. D. Cowan 1981).

It is necessary to adjust the core excitation energies according to accurate experimental or calculated values, since the uncertainty of the RCI and MCBP energies is about a few electronvolts (M. F. Gu 2003). The present $6 \leqslant n \leqslant 75$ resonance energies for Ca^{14+}, for both FAC and AS, are adjusted for an entire series according to the observed core excitation energies compiled in the Atomic Spectra Database of the National Institute of Standards and Technology (NIST; A. Kramida et al. 2020). In the present work, the RCI and MCBP energies are adjusted by around 0.6 eV.

The NIST-compiled ionization threshold for Ca^{13+} is from a relativistic multiconfiguration Dirac–Fock calculation (E. Biémont et al. 1999), which is 817.2(6) eV. However, it comes with a relatively large uncertainty. We have successfully used the relativistic many-body perturbation theory (RMBPT; M. F. Gu 2005; M. F. Gu et al. 2006) implemented in FAC (M. F. Gu 2008) to get high-precision energies for a series of HCIs (K. Wang et al. 2014, 2015, 2018a, 2018b, 2020; X. L. Guo et al. 2016; R. Si et al. 2016, 2018; C. Y. Zhang et al. 2018a, 2018b, 2021, 2022;

---

[9] https://github.com/flexible-atomic-code/fac/tree/master

J. Q. Li et al. 2019; Y. T. Li et al. 2020). In this work, the RMBPT method is used to calculate the ionization threshold of Ca^{13+}. In our RMBPT calculation for C-like Ca, all possible $1s^2 2l'^3 nl (l' \leqslant 1, n \leqslant 5, l \leqslant 4)$ configurations are contained in the M space, and all possible configurations that are generated from single or double excitations of the M space are included in the N space (M. F. Gu 2005; M. F. Gu et al. 2006). The maximum principal quantum numbers are respectively 150 and 70 for single and double excitations, and the maximum orbital quantum number is 20. Similarly, for N-like Ca, it is all the possible $1s^2 2l'^4 nl (l' \leqslant 1, n \leqslant 5, l \leqslant 4)$ contained in the M space. The ionization thresholds are obtained by calculating the energy difference between the ground state of a given ion and that of the next ionization stage. In the present RMBPT calculations, the ionization threshold of Ca^{13+} is 816.869 eV.

To monitor the convergence of the present calculations, we enlarge the electron correlation among all possible $1s^2 2l'^4 nl$ $(l' \leqslant 1, l < n)$ for Ca^{13+} by increasing n from 5 to 10 step by step. Most of the differences between the $n \leqslant 10$ and $n \leqslant 9$ individual resonance strengths are within 1%. Good convergence is achieved by $n = 10$.

3. Results and Discussion

The $\Delta n = 0$ resonance processes for C-like Ca recombining to N-like Ca give rise to three main resonance series, represented as

$$
\begin{aligned}
e^- + 2s^2 2p^2 [^3P_0] \\
\rightarrow
\begin{cases}
2s^2 2p^2 [^3P_{1,2};^1 D_2;^1 S_0] nl; \ \text{DR} \\
2s2p^3 [^5S_2;^3 D_{2,1,3};^3 P_{1,2,3};^1 D_2;^3 S_1;^1 P_1] nl; \ \text{DR}. \\
2p^4 [^3P_{2,1,0};^1 D_2;^1 S_0] nl. \ \text{TR}
\end{cases}
\end{aligned} \quad (7)
$$

Here, the DR process is associated with the doubly excited states $2s2p^3 nl$ and $2s^2 2p^2 nl$ formed by exciting single core electron $2s$ or $2p$ during the attachment of a free electron. In the trielectronic recombination process, two core electrons $2s^2$ are simultaneously excited to $2p$ orbital, forming triply excited intermediate states $2p^4 nl$.

In Figure 1, the old FAC (W. Q. Wen et al. 2020), old AS (W. Q. Wen et al. 2020), and new FAC multi-n CI results for Ca^{14+} are compared with the measured spectrum (W. Q. Wen et al. 2020) from 0 to 92 eV. The strong resonance peaks are labeled based on the new FAC multi-n CI calculation, and the core electrons $1s^2$ are omitted. A flattened Maxwellian electron energy distribution is used, as described in N. R. Badnell (2006), to obtain the present rate coefficients, where the parallel and perpendicular temperatures are respectively 0.33 meV and 12.4 meV, as determined by the experiment (W. Q. Wen et al. 2020). One can see that the new theoretical rate coefficients for Ca^{14+} are significantly improved over the old results. They reproduce well the experiment spectrum (W. Q. Wen et al. 2020) in the number of peaks and line profiles, especially for the resonances below 8 eV. In Figure 2, we compare the new FAC multi-n CI and new AS multi-n CI results, and we see that they are in good agreement with each other. The significant improvement in the present FAC and AS calculations is attributed to several aspects, including the effects of atomic radial potential, multi-n CI, and autoionization transitions near the threshold. See the detailed discussions below.

3.1. FAC Radial Potential

The old FAC results reported by W. Q. Wen et al. (2020) were calculated using a radial potential generated from all possible $1s^2 2l^4 (l \leqslant 1)$ configurations in the recombining ion (C-like). The corresponding orbital occupation numbers are 2, 1, 1, and 2 for $1s$, $2s$, $2p_{1/2}$, and $2p_{3/2}$ orbitals, respectively. Unfortunately, as shown in Figure 1, they poorly reproduce the measured spectrum (W. Q. Wen et al. 2020); in particular, they are missing the two important peaks at 0.40 eV/exp (0.28 eV/FAC)–0.50 eV/exp (0.43 eV/FAC) and 0.97 eV/exp (0.95 eV/FAC)–1.29 eV/exp (1.16 eV/FAC). Here (and hereafter), "exp" and "FAC" respectively represent the experimental and FAC-calculated energy positions.

In the new FAC calculations, the radial potential is generated from $1s^2 2l^5 (l \leqslant 1)$ configurations in the recombined ion (N-like). The orbital occupation numbers are 2, 1.125, 1.125, and 2.750 for $1s$, $2s$, $2p_{1/2}$, and $2p_{3/2}$ orbitals, respectively. Using the same occupation numbers, readers can reproduce this radial potential. With this potential, the new FAC results reproduce the measured spectrum well, especially for the resonances below 8 eV, agreeing with the experiment in both the number of peaks and line profiles. It can be found from Figure 1 that the two peaks at 0.40 eV/exp (0.28 eV/FAC)–0.50 eV/exp (0.43 eV/FAC) and 0.97 eV/exp (0.95 eV/FAC)–1.29 eV/exp (1.16 eV/FAC) not predicted by the old FAC calculation appear in our new results. These peaks are mainly associated with $2s2p^3 (^5S_2) 9l$.

In Table 1, we take the most important resonances between 0.97 eV/exp (0.95 eV/FAC) and 1.29 eV/exp (1.16 eV/FAC) from the old FAC and new FAC calculations as an example to demonstrate the effect of different potentials. The total autoionization rates $\sum_k A_{jk}^a$ from a resonance j to all possible autoionizing channels k, the total radiative decay rates $\sum_h A_{jh}^r$ from a resonance j to all possible lower levels h, and the resonance strength S_{ij} are listed. It is only possible for the resonances (j) around 1 eV listed in Table 1 to autoionize to the ground level $2s^2 2p^2 \, ^3P_0$, since the core excitation energy of the first excited level in Ca^{14+} is 2.1770 eV (A. Kramida et al. 2020), which is greater than the energies of the resonances (j) in Table 1. In this case, $A_{ji}^a = \sum_k A_{jk}^a$, i.e., both k and i are the ground state, and $\sum_f A_{if}^r = \sum_h A_{jh}^r$ in Equation (2), since DAC contributions are negligible.

It can be seen from Table 1 that the main contribution for resonances during 0.97 eV/exp (0.95 eV/FAC) and 1.29 eV/exp (1.16 eV/FAC) is from $2s^2 2p^2 (^3P_2) 28d$ (DR) resonance states in the old FAC calculation, which give quite weak resonance strengths, with only a few 10^{-20} cm^2eV. By contrast, in our new FAC calculations, the two resonance states $2s2p^3 (^5S_2) 9d_{5/2}$ (at 1.0948 eV) and $2s2p^3 (^5S_2) 9d_{3/2}$ (at 1.0967 eV) significantly contribute to the resonance strengths between 0.97 eV/exp (0.95 eV/FAC) and 1.29 eV/exp (1.16 eV/FAC), with greater than 100 10^{-20} cm^2 eV. However, the two important resonance states disappeared in our old FAC calculations. This is due to the poor potential used in the old FAC calculation, which results in the resonance energies of $2s2p^3 (^5S_2) 9l$ being below the ionization limit, so they do not give rise to any DR cross sections.

A similar case also occurs between 0.40 eV/exp (0.28 eV/FAC) and 0.50 eV/exp (0.43 eV/FAC). Again, the $2s2p^3 (^5S_2) 9p$ resonances were missed in the old FAC calculations but significantly contributed to our new FAC calculations. By using the radial potential generated from $1s^2 2l^5 (l \leqslant 1)$ configurations,
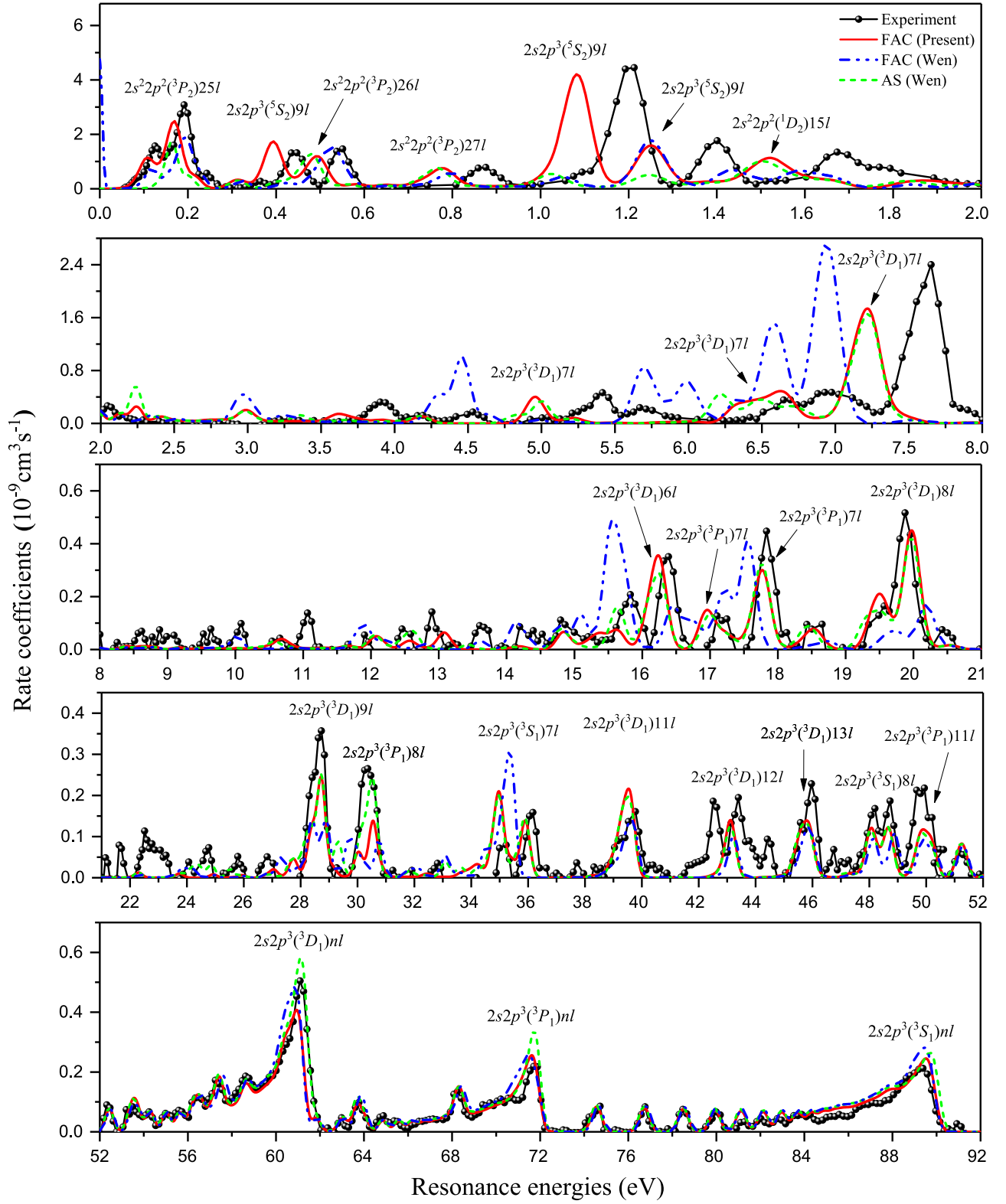
Figure 1. Comparison of the rate coefficients for Ca^{14+} from the old FAC (W. Q. Wen et al. 2020), old AS (W. Q. Wen et al. 2020), and new FAC multi-n CI calculations. The measured recombination spectrum (W. Q. Wen et al. 2020) is also presented. The strong resonance peaks are labeled based on the new FAC multi-n CI calculation, and the core electrons $1s^2$ are omitted.

the new FAC calculation from 2 to 92 eV is also improved over the old FAC results, which can be found in Figure 1.

In Figure 2, the new FAC multi-n CI and new AS multi-n CI results for Ca^{14+} are compared with the measured DR

spectrum (W. Q. Wen et al. 2020) from 0 to 92 eV. As we can see, the present FAC and AS calculations are cross-confirmed by each other well. They are generally in good agreement with each other, except for the resonances from
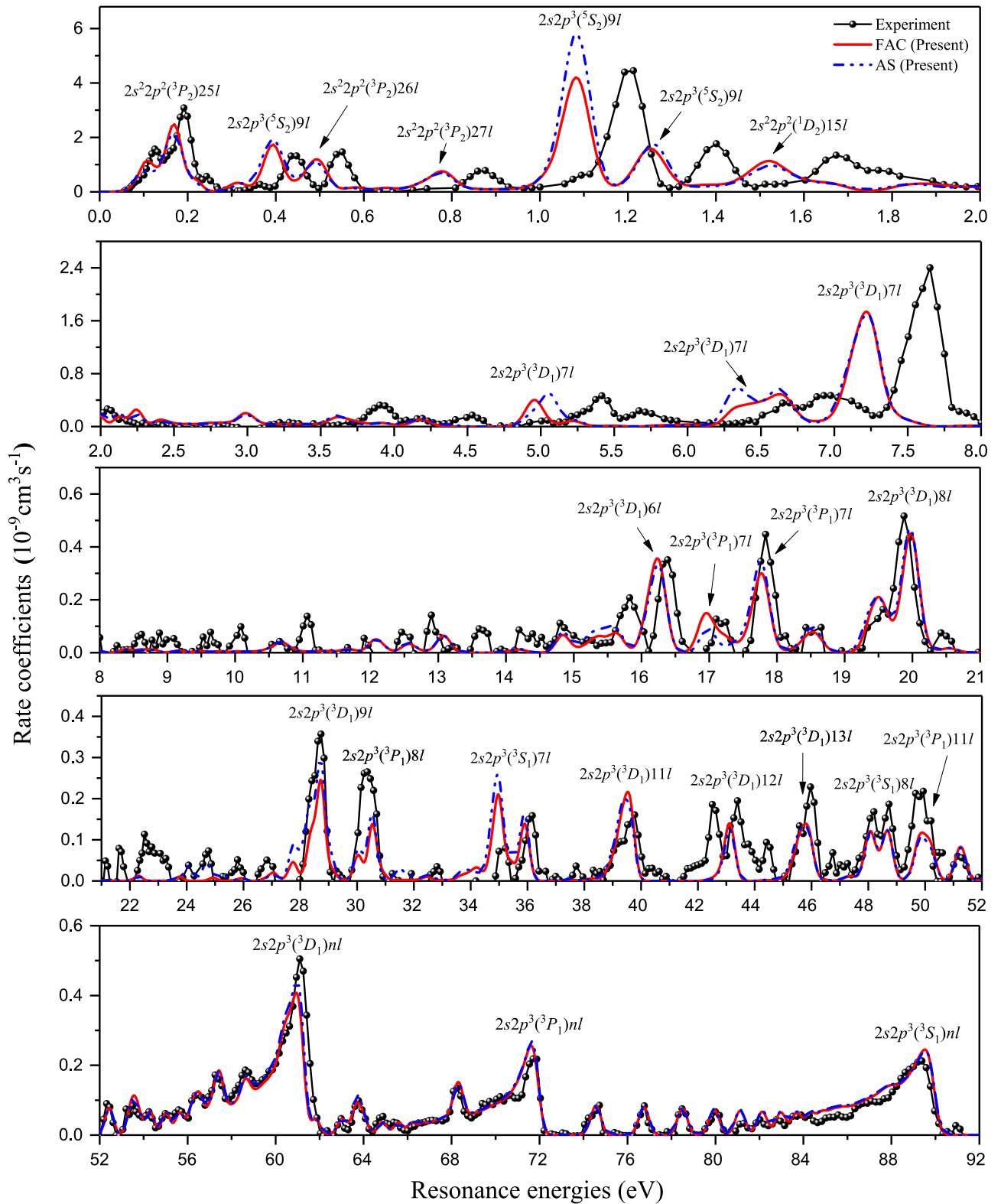
Figure 2. Comparison of the rate coefficients for Ca^{14+} from the present FAC multi-n CI and AS multi-n CI calculations. The measured recombination spectrum (W. Q. Wen et al. 2020) is also presented. The strong resonance peaks are labeled based on the present FAC calculation, and the core electrons $1s^2$ are omitted.

0.97 eV/exp (0.95 eV/FAC) to 1.29 eV/exp (1.16 eV/FAC), which are sensitive to different radial potentials used in FAC and AS calculations.

Due to the field ionization of weakly bound high-n Rydberg states, which occurs primarily due to the charge-separating dipole magnet, the estimated (hard) cutoff quantum number is $n_{cutoff} = 75$ in the experiment for Ca^{14+} (W. Q. Wen et al. 2020). From Figure 2, it can be seen that using the expected experimental $n_{cutoff} = 75$ leads to the present FAC and AS results that agree well with the measurement.
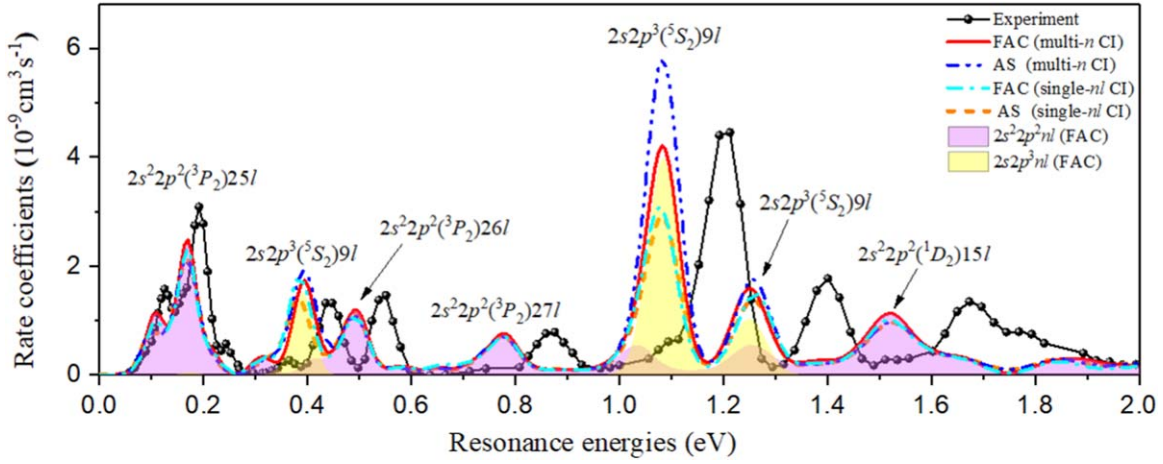
Figure 3. Comparison of the rate coefficients for Ca^{14+} from the present FAC single-nl CI, AS single-nl CI, FAC multi-n CI, and AS multi-n CI calculations. The measured recombination spectrum (W. Q. Wen et al. 2020) is also presented. The contributions from $2s^2 2p^2 nl$ and $2s2p^3 nl$ are also shown separately. The strong resonance peaks are labeled based on the new FAC multi-n CI calculation, and the core electrons $1s^2$ are omitted.

Table 1
Comparison of the Resonance Strengths (S_{ij}, in 10^{-20} cm^2 eV) of the Most Important Resonance States j Between 0.97/0.95 eV and 1.29/1.16 eV (Experimental/ FAC Positions) from the Old FAC, New FAC Single-nl CI, and New FAC Multi-n CI Calculations for Ca^{14+}

			Old FAC			New FAC Single-nl CI			New FAC Multi-n CI		
E_{ij}	Configuration	J^π	$\sum_k A_{jk}^a$	$\sum_h A_{jh}^r$	S_{ij}	A_{jk}^a	$\sum_h A_{jh}^r$	S_{ij}	A_{jk}^a	$\sum_h A_{jh}^r$	S_{ij}
1.0524	$2s^2 2p^2(^3P_2)28d_{5/2}$	$9/2^+$	0.23	0.09	1.58	0.20	0.17	2.16	0.16	0.21	2.20
1.0543	$2s^2 2p^2(^3P_2)28d_{3/2}$	$5/2^+$	1.87	0.18	2.34	1.86	0.31	3.84	2.07	0.37	4.45
1.0562	$2s^2 2p^2(^3P_2)28d_{3/2}$	$1/2^+$	4.97	0.40	1.73	5.03	0.65	2.73	5.07	0.76	3.14
1.0579	$2s^2 2p^2(^3P_2)28d_{5/2}$	$3/2^+$	20.5	0.25	2.30	19.5	0.47	4.37	20.0	0.50	4.62
1.0597	$2s^2 2p^2(^3P_2)28d_{5/2}$	$5/2^+$	3.56	0.29	3.76	3.67	0.55	6.77	3.35	0.57	6.96
1.0948	$2s2p^3(^5S_2)9d_{5/2}$	$5/2^-$	⋯	⋯	⋯	14.3	16.0	103	22.9	22.6	154
1.0967	$2s2p^3(^5S_2)9d_{3/2}$	$7/2^-$	⋯	⋯	⋯	65.2	16.5	239	99.4	22.3	328

Note. The resonance energies (E_{ij}, in eV), the autoionization rates $\sum_k A_{jk}^a$ (in 10^{10} s^{-1}) from j to k (where k represents all possible autoionizing channels from j), and the total radiative decay rates $\sum_h A_{jh}^r$ (in 10^{10} s^{-1}) from j to h (where h represents all possible lower levels of the transitions from j) are also given. ($A_{ji}^a = \sum_k A_{jk}^a$ and $\sum_f A_{jf}^r = \sum_h A_{jh}^r$ in Equation (2), since these resonance states can only autoionize decay to the ground state and DAC contributions are negligible.)

3.2. Effect of Multi-n CI

In Figure 3, the present new FAC single-nl CI and multi-n CI results are compared with the measured DR spectrum below 2 eV (W. Q. Wen et al. 2020). The new FAC single-nl CI and multi-n CI results at higher resonance energies are not shown here, because they are almost similar. From Figure 3, it can be seen that the resonance strengths from 0.97 eV/exp (0.95 eV/ FAC) to 1.29 eV/exp (1.16 eV/FAC) are obviously enhanced by the multi-n CI.

To analyze the effect of multi-n CI, we compare the most important resonance states between 0.97 eV/exp (0.95 eV/FAC) and 1.29 eV/exp (1.16 eV/FAC) from the new FAC single-nl CI and new FAC multi-n CI calculations in Table 1. For example, the autoionization rate A_{jk}^a from $2s2p^3(^5S_2)9d$ ($J = 7/2$) to the ground state is 6.52×10^{11} s^{-1} in the new FAC single-nl CI calculation, which is increased to 9.94×10^{11} s^{-1} (by a factor of 1.52) due to the multi-n CI. The total radiative decay rate $\sum_h A_{jh}^r$ from $2s2p^3(^5S_2)9d$ ($J = 7/2$) is increased by a factor of 1.35 (from 1.65×10^{11} s^{-1} to 2.23×10^{11} s^{-1}). Thus, the corresponding resonance strength S_{ij} is enhanced by a factor of 1.37 (from 2.39×10^{-18} cm^2 eV to 3.28×10^{-18} cm^2 eV), contributed by the multi-n CI. Similarly, the resonance strength S_{ij} of $2s2p^3(^5S_2)9d$ ($J = 5/2$) is enhanced by a factor of 1.49 (from 1.03×10^{-18} cm^2 eV to 1.54×10^{-18} cm^2 eV), also due to the

increase from both the autoionization rate and radiative decay rates.

The contributions from $2s^2 2p^2 nl$ and $2s2p^3 nl$ resonances are also separately shown in Figure 3. It can be seen that the resonance states $2s2p^3 nl$ strongly mix with $2s^2 2p^2 nl$, especially from 0.97 eV/exp (0.95 eV/FAC) to 1.29 eV/exp (1.16 eV/ FAC). For instance, the resonance state $2s2p^3(^5S_2)9d$ ($J = 7/2$) mainly mixes with $2s2p^3(^3P_1)6d$ ($J = 7/2$). Their mixing coefficients are 0.99 and 0.04, respectively. For the resonance state $2s2p^3(^5S_2)9d$ ($J = 5/2$), it mainly mixes with $2s2p^3$ ($^3P_1)6d$ ($J = 5/2$), and their mixing coefficients are 0.99 and 0.05, respectively. Once multi-n configuration mixing is considered in calculations, the radiative rates and autoionization rates will be redistributed according to their mixing weights. In this case, the mixing increases the autoionization rates and radiative decay rates. However, this form of mixing among the levels with different n is discarded in the single-nl calculation.

In Figure 3 and Table 2, we also compare the new AS single-nl CI and multi-n CI resonance strengths between 0.97 eV/exp (0.95 eV/AS) and 1.29 eV/exp (1.16 eV/AS). Here (and hereafter), "exp" and "AS" respectively represent the experimental and AS-calculated energy positions. The enhancement of resonance strengths over this resonance energy range due to the multi-n CI effect is also confirmed by our AS calculations.

Table 2
The Main Resonance States Lost in the Old AS Calculation for Ca^{14+} but Included in the New AS Single-nl CI and New AS Multi-n CI Calculations

E_{ij}	Configurations	J^π	New AS Single-nl CI			New AS Multi-n CI		
			$\sum_k A^a_{jk}$	$\sum_h A^r_{jh}$	S_{ij}	A^a_{jk}	$\sum_h A^r_{jh}$	S_{ij}
0.3872	$2s2p^3(^5S_2)9p$	$5/2^+$	3.29	7.99	86.8	4.19	14.9	88.2
0.3919	$2s2p^3(^5S_2)9p$	$3/2^+$	0.55	8.01	12.6	0.77	15.0	13.0
0.3972	$2s2p^3(^5S_2)9p$	$1/2^+$	89.9	8.04	89.5	65.0	15.1	104
1.0948	$2s2p^3(^5S_2)9d$	$5/2^-$	14.1	15.7	97.1	36.1	31.4	192
1.0952	$2s2p^3(^5S_2)9d$	$3/2^-$	0.18	15.5	1.55	0.63	32.1	4.70
1.0961	$2s2p^3(^5S_2)9d$	$1/2^-$	0.37	15.3	1.59	1.31	32.7	4.89
1.0967	$2s2p^3(^5S_2)9d$	$7/2^-$	63.6	16.3	229	154	30.8	398
1.2652	$2s2p^3(^5S_2)9f$	$3/2^+$	29.3	4.86	32.7	37.8	6.44	43.1
1.2817	$2s2p^3(^5S_2)9f$	$9/2^+$	1.53	4.86	22.8	2.76	6.44	37.3
1.2821	$2s2p^3(^5S_2)9f$	$5/2^+$	13.0	4.86	41.6	16.8	6.44	53.9

Note. The resonance strengths (S_{ij}, in 10^{-20} cm^2 eV) of the most important resonance states j between 0.38 and 1.27 eV from the new AS single-nl CI and new AS multi-n CI calculations are also presented. The resonance energies (E_{ij}, in eV), the autoionization rates $\sum_k A^a_{jk}$ (in 10^{10} s^{-1}) from j to k (where k represents all possible autoionizing channels from j), and the total radiative decay rates $\sum_h A^r_{jh}$ (in 10^{10} s^{-1}) from j to h (where h represents all possible lower levels of the transitions from j) are also given. ($A^a_{ji} = \sum_k A^a_{jk}$ and $\sum_f A^r_{jf} = \sum_h A^r_{jh}$ in Equation (2), since these resonance states can only autoionize decay to the ground state and DAC contributions are negligible.)

For the resonance states j listed in Table 2, $A^a_{ji} = \sum_k A^a_{jk}$ and $\sum_f A^r_{jf} = \sum_h A^r_{jh}$ in Equation (2), since these resonance states can only autoionize decay to the ground state and cascade transitions are negligible. Also for $2s2p^3(^5S_2)9d$ ($J = 7/2$), the autoionization rate $\sum_k A^a_{jk}$ from $2s2p^3(^5S_2)9d$ ($J = 7/2$) to the ground state is 6.36×10^{11} s^{-1} in the new AS single-nl CI calculation, which is increased to 1.54×10^{12} s^{-1} (by a factor of 2.42) due to the multi-n CI. The total radiative decay rate $\sum_h A^r_{jh}$ from $2s2p^3(^5S_2)9d$ ($J = 7/2$) is increased by a factor of 1.89 (from 1.63×10^{11} s^{-1} to 3.08×10^{11} s^{-1}). Thus, the resonance strength S_{ij} of $2s2p^3(^5S_2)9d$ ($J = 7/2$) is increased by a factor of 1.74 (from 2.29×10^{-18} cm^2 eV to 3.98×10^{-18} cm^2 eV), contributed by the multi-n CI. Similarly, the resonance strength S_{ij} of $2s2p^3(^5S_2)9d$ ($J = 5/2$) is enhanced by a factor of 1.98 (from 9.71×10^{-19} cm^2 eV to 1.92×10^{-18} cm^2 eV), also due to the increase from both the autoionization rate and radiative decay rates.

3.3. Autoionization Transitions near Threshold

From Figure 1, it can be seen that the three important resonance peaks at 0.40 eV/exp (0.28 eV/AS)–0.50 eV/exp (0.43 eV/AS), 0.97 eV/exp (0.95 eV/AS)–1.29 eV/exp (1.16 eV/AS), and 1.30 eV/exp (1.16 eV/AS)–1.49 eV/exp (1.32 eV/AS) have almost disappeared in our old AS calculation. This is due to the energies of the target levels explicitly calculated in the AS procedure generally being a little too low, and so the resonance states between threshold and 1.3 eV ($2s2p^3(^5S_2)9l$) were calculated to lie just below the ionization limitation. Thus, no autoionization data were calculated for them in the old AS calculation. Adjusting to observed target energies is a post-processing exercise that can move existing resonance positions, including discarding any predicted to be true bound, but does not create missing resonances. Instead, the continuum should have been slightly lowered in the AS calculation to ensure that all potential autoionization data exist for low-lying states in the first place. It was not done in the old AS calculation; the continuum energies were only adjusted in the AS post-processor. In the new AS calculations, we lower the continuum by 0.3 Ryd to ensure any resonances near the ionization threshold are not omitted at this point. They may be discarded later by the AS post-processor if

they are still bound after shifting back the continuum to the correct position in combination with using observed/accurate theoretical target energies. With this procedure, the resonance states $2s2p^3(^5S_2)9l$ that were below 1.3 eV are present in the new AS calculations, and their final position is determined by the use of the observed target energies. Their resonance information is presented in Table 2. As we can see from Table 2 and Figure 3, the resonance states $2s2p^3(^5S_2)9l$ give large contributions to the spectrum at 0.40 eV/exp (0.28 eV/AS)–0.50 eV/exp (0.43 eV/AS), 0.97 eV/exp (0.95 eV/AS)–1.29 eV/exp (1.16 eV/AS), and 1.30 eV/exp (1.16 eV/AS)–1.49 eV/exp (1.32 eV/AS).

3.4. Remaining Issues

The present FAC and AS calculations for Ca^{14+} are in much better agreement with the experimental DR resonance spectrum in detail than previous calculations (W. Q. Wen et al. 2020). The resonance energies that are decided by an RF coming from the same core excitation energy should show a regular shift with the experimental DR spectrum. However, there is still an irregular shift between the present calculated resonance energies and the experimental positions (W. Q. Wen et al. 2020), as shown in Figures 1, 2, and 3. For example, the positions of the strongest resonances for $2s2p^3(^5S_2)9l$ from calculations and the experiment are 0.37 eV/0.44 eV (with a difference of 0.07 eV), 1.06 eV/1.20 eV (with a difference of 0.14 eV), and 1.26 eV/1.40 eV (with a difference of 0.14 eV), respectively. The positions of the strongest resonances for $2s^22p^2(^3P_2)25l$, $2s^22p^2(^3P_2)26l$, and $2s^22p^2(^3P_2)27l$ from calculations and the experiment are 0.16 eV/0.19 eV (with a difference of 0.03 eV), 0.48 eV/0.54 eV (with a difference of 0.06 eV), and 0.77 eV/0.87 eV (with a difference of 0.10 eV), respectively.

Describing the position of low-energy resonances challenges both theory and experiment. It should be noted that the NIST core excitation energies (A. Kramida et al. 2020) are used in the present calculations of the resonance energies. For example, the core configurations related to the spectrum below 8 eV and their NIST energies are $2s^22p^2\,^3P_2$ (4.4539 eV), $2s^22p^2\,^1D_2$ (13.465 eV), $2s2p^3\,^5S_2$ (34.21 eV), and $2s2p^3\,^3D_1$ (61.691 eV). It should be noted that the energy 34.21 eV of $2s2p^3\,^5S_2$ (see

Figure 1, top panel) is characterized as being "determined by interpolation or extrapolation of known experimental values or by sem-empirical calculation" (A. Kramida et al. 2020). On the experimental side, as mentioned in W. Q. Wen et al. (2020), the whole DR spectrum of Ca^{14+} was measured in three scanning modes of the electron energy fast-detuning system. The center-of-mass collision energies between electrons and ions were calculated using the added detuning voltage at the electron cooler. Consequently, some possible irregular shifts in experimental positions at energies lower than 8 eV may be attributed to potential inaccuracies in energy calibration during the experimental measurement. If we shift the resonance energies to some extent, the experimental and theoretical spectra lower than 8 eV could match each other well.

As we can see from Figure 2, the present FAC and AS resonance strengths still differ somewhat from measurements at higher resonance energies, such as at ~17.8, ~28.5, ~30.5, ~34.9, ~45.9, ~48.1, ~48.7, and ~49.8 eV. We note that strong electron correlations, such as those between $2s2p^39l$ and $2p^45l$, as well as between $2s2p^38l$ and $2p^45l$, come into play here. The electron correlations between $2s2p^38l$ and $2s2p^314l$ are also expected to contribute to the resonance strengths between 48 and 49 eV, since their resonance energies are quite close. However, it is difficult to include such large-scale electron correlations up to $n = 14$ in the current FAC calculations.

It should also be noted that many weak resonance peaks appear in the measured spectrum between 8 and 52 eV, but they are not shown in the present calculations. In the experiment (W. Q. Wen et al. 2020), the particle detector was partly damaged during the DR experiment on Ca^{14+} (W. Q. Wen et al. 2020). As a result, the statistics of experimental measurements are not as good as the experiment on Ar^{14+} (Z. K. Huang et al. 2018). Further investigations are needed in the future.

3.5. Plasma Rate Coefficients

The present $\Delta n = 0$ plasma rate coefficients obtained from the new FAC and AS multi-n CI calculations for Ca^{14+} are compared with the results derived from the measurements (W. Q. Wen et al. 2020) in Figure 4. The old FAC and AS results are the same as provided in W. Q. Wen et al. (2020). The FAC results from M. F. Gu (2003) are also presented for comparison. It should be noted that our old AS results are the same as the AS results from O. Zatsarinny et al. (2004b) that are compiled on the UK APAP website. The vertical dashed bars denote the boundaries of the PP and CP temperature ranges, defined to be where the fractional abundance of this ion is 10% of its maximum (T. Kallman & M. Bautista 2001; P. Bryans et al. 2009).

From Figure 4, we can see that our new FAC and AS plasma rate coefficients for Ca^{14+} are in good agreement with each other to 10% from 0.1 to 0.3 eV, to 5% from 0.3 to 5 eV, which covers the PP temperature range, and to 3% from 5 to 1000 eV, which covers the CP temperature range. Both agree also with the experiment to within 20% over the temperature range from 2.6 to 34.5 eV, where Ca^{14+} is expected to be abundant in PP. But the old AS results are lower than the experiment by up to 40%—this is exacerbated by the rate coefficient falling off rapidly with the temperature here. Over the CP temperature range, our new FAC and AS results reproduce the experiment within 2%, while the old FAC and AS ones deviate from the experiment by up to 10%.
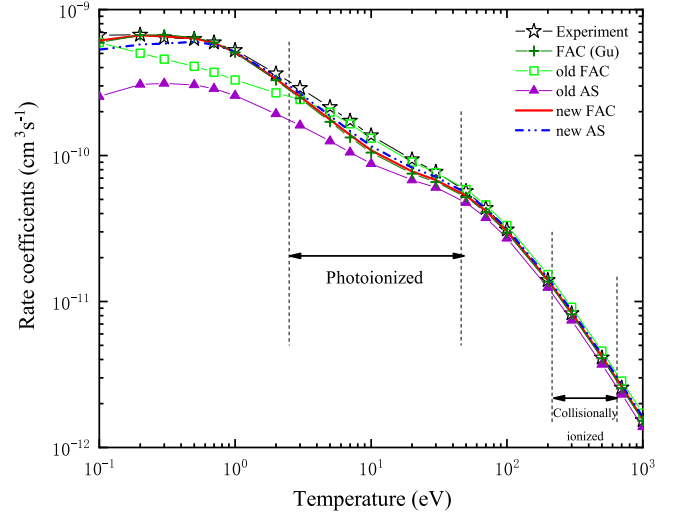

Figure 4. Comparison of the plasma rate coefficients for Ca^{14+} from old FAC (W. Q. Wen et al. 2020), old AS (W. Q. Wen et al. 2020), new FAC multi-n CI, and new AS multi-n CI calculations with the experimentally derived values (W. Q. Wen et al. 2020). The FAC results from M. F. Gu (2003) are also presented. The vertical dashed bars denote the boundaries of the PP and CP temperature ranges.

Table 3
The Fitted Coefficients c_i (in 10^{-10} cm^3 s^{-1}) and E_i (in eV) for the Present Multi-n CI Plasma Rate Coefficients of $\Delta n = 0$ Channels for C-like Ca^{14+}

No.	c_i	E_i
1	1.58[0]	2.25[−1]
2	1.28[1]	1.22[0]
3	2.80[1]	5.90[0]
4	9.07[1]	2.42[1]
5	4.09[2]	6.99[1]

Note. The numbers in the squared brackets are powers of 10.

There is only a few percent difference between the old FAC results (W. Q. Wen et al. 2020) and the experiment (W. Q. Wen et al. 2020) over the PP temperature range. This level of agreement in the total rate coefficient is fortuitous, because the unique potential chosen in the old FAC calculation causes many resonance strengths to be overestimated in the detailed comparison with the experiment, as we have shown (see Section 3.1). Agreement to within 3% is also found between the FAC results from M. F. Gu (2003) and the present calculations, since the effect of multi-n CI is small here. But, as we have just seen, such a level of agreement can be fortuitous. There are no detailed FAC results from M. F. Gu (2003) to compare with the observed detailed DR resonance spectrum for Ca^{14+} (W. Q. Wen et al. 2020) to see if this is so or not. It is also worth mentioning that our DR calculations for C-like Ar^{12+} (S. Mahmood et al. 2020) and C-like Kr^{30+} (W.-L. Ma et al. 2023) were found to be in good agreement with the detailed experimental measurements, for which we used the same calculation strategies as the present work for C-like Ca^{14+}.

The present work only focuses on studying $\Delta n = 0$ channels. The $\Delta n = 1$ plasma rate coefficients can be found in our previous AS calculations (O. Zatsarinny et al. 2004b).

To make it convenient to use the present $\Delta n = 0$ plasma rate coefficients in plasma modeling, the present plasma rate

coefficients are fitted by

$$\alpha(T_e) = T_e^{-3/2} \sum_i c_i \times \exp\left(-\frac{E_i}{T_e}\right). \qquad (8)$$

We give the fit parameters of c_i and E_i for the present AS results for Ca^{14+} in Table 3, and they can reproduce the present results within 2% from 0.3 eV up to 1000 eV.

4. Conclusion

The present DR rate coefficients for Ca^{14+} are calculated with the RDW approximation implemented in the FAC and the SRDW approximation implemented in the AS. The reasons behind the large discrepancies between the previous theoretical and experimental spectra as well as the differences among various theoretical results are clearly revealed. The present FAC and AS results are significantly improved over the previous calculations, especially for the resonance spectrum below 8 eV, agreeing well with the experiment in the number of peaks and line profiles. The present FAC and AS plasma rate coefficients of Ca^{14+} agree with the experiment within $\sim$20% and $\sim$2% in the PP and CP temperature ranges, respectively. The present FAC and AS results also cross-confirmed each other excellently, and the differences between them are within 5% in the PP and CP temperature ranges.

Moreover, in the FAC calculations for DR rate coefficients, a radial potential generated from the configurations in recombined ions ($(N+1)$-electrons) is recommended, instead of that generated from the configurations in recombining ions (N-electrons). In AS calculations for autoionization rates, the ionization limit may need to be lowered slightly to ensure that all potential autoionization data exist for low-lying states. Not all users did so in the past. These findings can be used to improve the calculations for other L-shell ions.

Although the present FAC and AS results are in much better agreement with the detailed experimental DR resonance spectrum than previous calculations, there are still some differences in resonance energies and strengths at low energy, which may be due to difficulties experienced during the experiment. Further theoretical and experimental investigations would be helpful in this context.

The present theoretical calculations provide benchmarked DR data for Ca^{14+} with much less uncertainty than before, and greatly improved detailed agreement with the experiment, which can be expected to be found for other similar elements/ charges. This is in contrast to the agreement found in total DR rate coefficients, which may be fortuitous for one ion but cannot be relied upon to hold for any other ion. This gives confidence to data users modeling non–local thermodynamic equilibrium plasmas in determining the ionization balance, line emission, thermal structure, and ionization structures of PP and CP plasmas more widely.

ORCID iDs

C. Y. Zhang ⓘ https://orcid.org/0000-0003-1935-6907
B. S. Yan ⓘ https://orcid.org/0009-0008-3465-2695
K. Wang ⓘ https://orcid.org/0000-0001-6998-1693
K. Yao ⓘ https://orcid.org/0000-0002-9083-8477
W. Q. Wen ⓘ https://orcid.org/0000-0001-5266-3058
X. W. Ma ⓘ https://orcid.org/0000-0001-9831-0565
L. F. Zhu ⓘ https://orcid.org/0000-0002-5771-0471

References

Altun, Z., Yumak, A., Badnell, N. R., Colgan, J., & Pindzola, M. S. 2004, A&A, 420, 775
Badnell, N. R. 2006, JPhB, 39, 4825
Badnell, N. R. 2007, JPhCS, 88, 12070
Badnell, N. R. 2011, CoPhC, 182, 1528
Badnell, N. R., O'Mullane, M. G., Summers, H. P., et al. 2003, A&A, 406, 1151
Badnell, N. R., & Zhang, C. Y. 2024, EPJD, 78, 84
Bautista, M. A., & Kallman, T. R. 2001, ApJS, 134, 139
Biémont, E., Frémat, Y., & Quinet, P. 1999, ADNDT, 71, 117
Bryans, P., Badnell, N. R., Gorczyca, T. W., et al. 2006, ApJS, 167, 343
Bryans, P., Landi, E., & Savin, D. W. 2009, ApJ, 691, 1540
Burgess, A. 1964, ApJ, 139, 776
Burgess, A., Mason, H. E., & Tully, J. A. 1989, A&A, 217, 319
Colgan, J., Pindzola, M. S., & Badnell, N. R. 2004, A&A, 417, 1183
Colgan, J., Pindzola, M. S., Whiteford, A. D., & Badnell, N. R. 2003, A&A, 412, 597
Cowan, R. D. 1981, The Theory of Atomic Structure and Spectra (Berkeley, CA: Univ. California Press)
Del Zanna, G., Dere, K. P., Young, P. R., & Landi, E. 2021, ApJ, 909, 38
Dere, K. P., Del Zanna, G., Young, P. R., Landi, E., & Sutherland, R. S. 2019, ApJS, 241, 22
Ferland, G. J., Korista, K. T., Verner, D. A., et al. 1998, PASP, 110, 761
Foster, A. R., Ji, L., Smith, R. K., & Brickhouse, N. S. 2012, ApJ, 756, 128
Gu, M. F. 2003, ApJ, 590, 1131
Gu, M. F. 2005, ApJS, 156, 105
Gu, M. F. 2008, CaJPh, 86, 675
Gu, M. F., Holczer, T., Behar, E., & Kahn, S. M. 2006, ApJ, 641, 1227
Guo, X. L., Si, R., Li, S., et al. 2016, PhRvA, 93, 012513
Hitomi Collaboration, Aharonian, F., Akamatsu, H., et al. 2016, Natur, 535, 117
Hitomi Collaboration, Aharonian, F., Akamatsu, H., et al. 2017, Natur, 551, 478
Hitomi Collaboration, Aharonian, F. A, Akamatsu, H., et al. 2018, PASJ, 70, 12
Huang, Z. K., Wen, W. Q., Xu, X., et al. 2018, ApJS, 235, 2
Kallman, T., & Bautista, M. 2001, ApJS, 133, 221
Kallman, T. R., & Palmeri, P. 2007, RvMP, 79, 79
Khan, N., Huang, Z.-K., Wen, W.-Q., et al. 2018, ChPhC, 42, 064001
Kramida, A., Ralchenko, Y., Reader, J. & NIST ASD Team 2020, NIST Atomic Spectra Database (v5.8) (Gaithersburg, MD: National Institute of Standards and Technology)
Li, J. Q., Zhang, C. Y., Si, R., Wang, K., & Chen, C. Y. 2019, ADNDT, 126, 158
Li, Y. T., Si, R., Li, J. Q., et al. 2020, ADNDT, 133, 101339
Ma, W.-L., Wang, S.-X., Huang, Z.-K., et al. 2023, JPhB, 56, 095203
Mahmood, S., Huang, Z. K., Wen, W. Q., et al. 2020, JPhB, 53, 085004
Meng, F.-C., Chen, C.-Y., Shi, X.-H., et al. 2007, JPhB, 40, 4269
Mitnik, D. M., & Badnell, N. R. 2004, A&A, 425, 1153
Orban, I., Böhm, S., Loch, S. D., & Schuch, R. 2008, A&A, 489, 829
Orban, I., Loch, S. D., Böhm, S., & Schuch, R. 2010, ApJ, 721, 1603
Peleg, A., Behar, E., Mandelbaum, P., & Schwob, J. L. 1998, PhRvA, 57, 3493
Pindzola, M. S., Badnell, N. R., & Griffin, D. C. 1992, PhRvA, 46, 5725
Schippers, S., Schnell, M., Brandau, C., et al. 2004, A&A, 421, 1185
Schnell, M., Gwinner, G., Badnell, N. R., et al. 2003, PhRvL, 91, 043001
Si, R., Li, S., Guo, X. L., et al. 2016, ApJS, 227, 16
Si, R., Zhang, C. Y., Cheng, Z. Y., et al. 2018, ApJS, 239, 3
Tashiro, M., Maejima, H., Toda, K., et al. 2018, Proc. SPIE, 10699, 1069922
Wang, K., Guo, X. L., Liu, H. T., et al. 2015, ApJS, 218, 16
Wang, K., Jönsson, P., Gaigalas, G., et al. 2018a, ApJS, 235, 27
Wang, K., Jönsson, P., Zanna, G. D., et al. 2020, ApJS, 246, 1

Wang, K., Li, D. F., Liu, H. T., et al. 2014, ApJS, 215, 26
Wang, K., Song, C. X., Jönsson, P., et al. 2018b, ApJS, 239, 30
Wang, S. X., Huang, Z. K., Wen, W. Q., et al. 2019, A&A, 627, A171
Wang, S. X., Xu, X., Huang, Z. K., et al. 2018, ApJ, 862, 134
Wen, W. Q., Huang, Z. K., Wang, S. X., et al. 2020, ApJ, 905, 36
Zanna, G. D., & Mason, H. E. 2018, LRSP, 15, 5
Zatsarinny, O., Gorczyca, T. W., Fu, J., et al. 2006, A&A, 447, 379
Zatsarinny, O., Gorczyca, T. W., Korista, K. T., Badnell, N. R., & Savin, D. W. 2003, A&A, 412, 587

Zatsarinny, O., Gorczyca, T. W., Korista, K., Badnell, N. R., & Savin, D. W. 2004a, A&A, 426, 699
Zatsarinny, O., Gorczyca, T. W., Korista, K. T., Badnell, N. R., & Savin, D. W. 2004b, A&A, 417, 1173
Zhang, C. Y., Li, J. Q., Wang, K., et al. 2022, PhRvA, 105, 022817
Zhang, C. Y., Si, R., Liu, Y. W., et al. 2018a, ADNDT, 121, 256
Zhang, C. Y., Si, R., Yao, K., et al. 2018b, JQSRT, 206, 180
Zhang, C. Y., Wang, K., Si, R., et al. 2021, JQSRT, 269, 107650
Zhang, C. Y., Wu, S. J., Wang, K., et al. 2023, PhRvA, 108, 022801